Geochemistry Geophysics Geosystems G3

Article
Volume 15, Number 1
23 January 2014
doi: 10.1002/2013GC004936
ISSN: 1525-2027

Published by AGU and the Geochemical Society

A method for estimating ice mass loss from relative InSAR observations: Application to the Vatnajökull ice cap, Iceland

Wenliang Zhao, Falk Amelung, Timothy H. Dixon, Shimon Wdowinski, and Rocco Malservisi

Division of Marine Geology and Geophysics, Rosenstiel School of Marine and Atmospheric Science, University of Miami, 4600 Rickenbacker Causeway, Miami, Florida 33149, USA

School of Geosciences, University of South Florida, Tampa, Florida, USA (famelung@rsmas.miami.edu)

[1] We present a new method for estimating ice mass loss from glaciers and ice sheets using Interferometric Synthetic Aperture Radar (InSAR) time-series data. We use a linear inversion method based on observations of nearby bedrock uplift and a solution for surface loading of an elastic half-space. The method assumes that mass loss is focused on lower elevation terminal regions of the glacier or ice sheet, and that there is an exponential decrease in thinning rate toward the higher elevation interior. We apply the method to uplift rates between 1995 and 2009 near Vatnajökull, Iceland. The data reveal up to 13 mm/yr relative line-of-sight (LOS) velocity around the south-western edge of Vatnajökull. We find an ice mass loss rate of $6.8^{+0.8}_{-0.7}$ Gt/yr, in approximate agreement with other estimates. Ice loss since 1995 is twice as fast as the loss rate estimated for the rest of the 20th century.

Components: 12,288 words, 7 figures, 1 table.

Keywords: InSAR; time series; ice mass balance; elastic half-space; Young's Modulus.

Index Terms: 1240 Satellite geodesy: results: Geodesy and Gravity; 1218 Mass balance: Geodesy and Gravity; 1223 Ocean/Earth/atmosphere/hydrosphere/cryosphere interactions: Geodesy and Gravity; 1236 Rheology of the lithosphere and mantle: Geodesy and Gravity; 6929 Ionospheric physics: Radio Science; 7215 Earthquake source observations: Seismology; 7230 Seismicity and tectonics: Seismology; 7240 Subduction zones: Seismology; 1631 Land/atmosphere interactions: Global Change; 1836 Hydrological cycles and budgets: Hydrology; 1843 Land/atmosphere interactions: Hydrology; 3010 Gravity and isostasy: Marine Geology and Geophysics; 3322 Land/atmosphere interactions: Atmospheric Processes; 4532 General circulation: Oceanography: Physical; 8160 Rheology: general: Tectonophysics; 0762 Mass balance: Cryosphere; 0758 Remote sensing: Cryosphere.

Received 10 July 2013; **Revised** 5 November 2013; **Accepted** 18 November 2013; **Published** 23 January 2014.

Zhao, W., F. Amelung, T. H. Dixon, S. Wdowinski, and R. Malservisi (2014), A method for estimating ice mass loss from relative InSAR observations: Application to the Vatnajökull ice cap, Iceland, *Geochem. Geophys. Geosyst.*, *15*, 108–120, doi:10.1002/2013GC004936.

1. Introduction

[2] The mass balance of ice sheets, ice caps, and glaciers is one expression of global climate change. Many recent studies suggest rapid acceleration of cryosphere melting since the late 1990s [*Khan et al.*, 2007, 2010; *Howat et al.*, 2008; *Wouters et al.*, 2008; *Chen et al.*, 2009; *Jiang et al.*, 2010; *Sørensen et al.*, 2011; *Ewert et al.*, 2011; *Shepherd et al.*, 2012; *Lenaerts et al.*, 2013; *Yang et al.*, 2013]. Ice loss currently contributes 0.7–1.8 mm/yr to present-day global sea

© 2013. American Geophysical Union. All Rights Reserved.

level rise [*Meier et al*., 2007; *Gardner et al*., 2013] and this is likely to increase in the future.

[3] Space geodetic techniques commonly used to estimate ice mass balance include the Gravity Recovery and Climate Experiment (GRACE) [*Velicogna and Wahr*, 2006; *Chen et al*., 2006; *Ramillien et al*., 2006; *Wouters et al*., 2008; *Slobbe et al*., 2009] and laser and radar altimetry [*Howat et al*., 2008; *Pritchard et al*., 2009; *Sørensen et al*., 2011]. These techniques typically have limited spatial resolution. InSAR and speckle tracking can be used to measure ice flow velocities and their temporal changes [*Joughin*, 2002; *Rignot et al*., 2011b, 2013] from which, combined with ice thickness data and regional models, changes in mass balance can be inferred [*Rignot et al*., 2008; *Osmanoğlu et al.*, 2013]. The main challenge of InSAR-based ice flow measurements is poor temporal resolution (sampling intervals of several weeks), although this recently was improved with the launch of TerraSAR-X [*Joughin et al*., 2011]. InSAR and GPS have also been used to directly measure uplift at the edge of glaciers [*Jiang et al*., 2010; *Bevis et al*., 2012; *Liu et al*., 2012; *Auriac et al*., 2013; *Yang et al*., 2013], from which mass balance can be inferred, as described below.

[4] The mass loss of a glacier results in uplift of nearby crust, due to isostasy and local deformation, a process known as glacial isostatic adjustment (GIA). Hence, uplift measurements can constrain mass balance [e.g., *Jiang et al*., 2010]. However, these methods have two limitations. First, they require independent information (or assumptions) on load distribution in areas where no geodetic observations are available, for example assuming a homogenous unloading slab [*Jiang et al*., 2010]. Second, the observed ground deformation consists of both an instantaneous elastic and a delayed viscous component (Figure 1) [e.g., *Peltier*, 1974; *Wu*, 1992; *Mitrovica et al*., 2001]. The elastic deformation can be assumed to represent contemporaneous uplift in response to current melting. The viscous deformation may have two components, a long delayed component due to melting of ice sheets from Earth's last glacial maximum, approximately 20,000 years ago, and a more recent component in response to the early phases of the current melting period. For example, in Iceland, the current melting period started at the end of the Little Ice Age at ~1890 AD [*Sigmundsson*, 1991]. This is long enough before present that viscous response of the lower crust and upper mantle might contribute to the contemporary surface deformation field. The viscous component has a long-wavelength signal (spatial extent larger than 40 km) because it occurs in response to flow in the mantle (mainly below 40 km). The interpretation of ground deformation in terms of mass balance requires separation of these various spatial and temporal components [*Jiang et al*., 2010; *Bevis et al*., 2012].

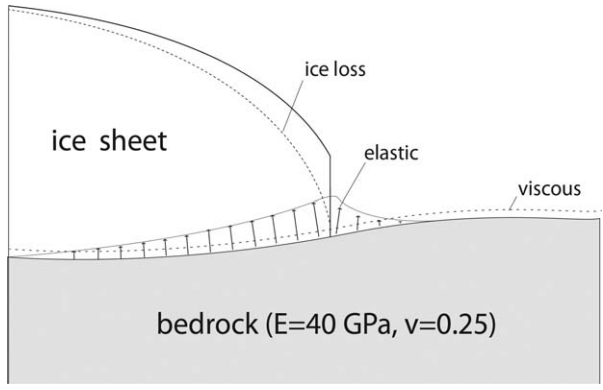

Figure 1. Schematic illustration summarizing the ice mass loss estimation approach. Glacial isostatic adjustment (GIA) has two components, contemporaneous elastic response due to current melting and longer-term viscous response due to prior melting and early phases of current melting. Melting at the edge of an ice sheet results in short wavelength elastic response, whereas viscous response is a longer-wavelength signal. Relative InSAR measurements are sensitive to short but not to long wavelength signal. The method works only for ice loss along the ice edge where elastic response has much shorter wavelength than viscous response. We use an elastic half-space model with a Young's modulus of 40 GPa and Poisson's ratio of 0.25. Shrinking of the ice cap surface area is exaggerated.

[5] This paper presents a new approach for mass balance estimation from geodetic observations (Figure 1). We use InSAR, which measures relative displacements across a SAR scene and is sensitive to local deformation differences. Since ice melting occurs primarily at lower elevations near the ice edge, the short wavelength contemporaneous deformation (spatial extent a few tens of kilometers or less), is resolvable with InSAR and is dominated by the contemporary elastic component of deformation.

[6] The paper is organized as follows. We first describe the geological background (section 2.) and then introduce the theory of our ice mass loss estimation method (section 3.). We then present the InSAR observations and ice mass loss estimation for the Vatnajökull ice cap in Iceland (sections 4. and 5.), followed by a discussion of the sensitivity and potential error sources for the technique (section 6.).

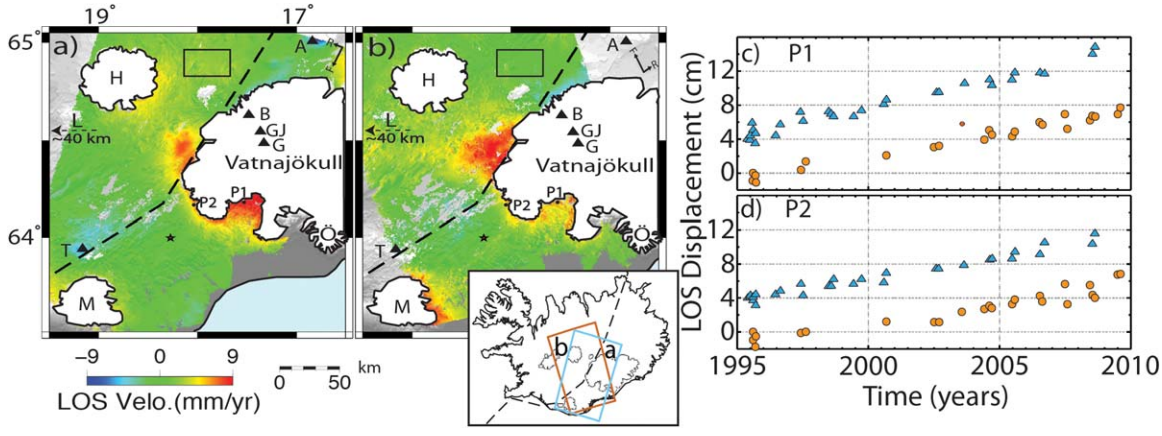

Figure 2. Averaged 1995–2009 LOS velocities around Vatnajökull from (a) descending track 281 and (b) ascending track 316 and location map. Dashed line marks mid-Atlantic ridge. Star marks the reference point (near GPS station 7485). Black rectangle (east of H): area used for error estimation. A, B, G, GJ, Ö, T: Askja, Bardarbunga Grimsvötn, Gjalp, Oraefajökull, Torfajökull volcanoes. H, L, M: Hofsjökull, Langjökull and Myrdalsjökull ice caps. (c and d) LOS displacement time series for locations P1 and P2. Blue triangles: descending orbit (shifted upward 4 mm/yr for visualization). Red circles: ascending orbit. Arrows at lower right corners of Figures 2a and 2b indicate flight directions (F) and the range (R = LOS) directions. Background of Figures 2a and 2b shows DEM of the study area.

2. Background

[7] The Icelandic ice caps were the 7th largest contributor to global sea level rise between 2003 and 2010 [*Jacob et al*., 2012]. Vatnajökull is the largest ice cap in Iceland, with a mean elevation of 1215 m and a maximum ice thickness of 950 m [*Björnsson and Pálsson*, 2008]. The other three big Icelandic ice caps, Hofsjökull, Mýrdalsjökull, and Langjökull, are located further west (Figure 2). The western part of Vatnajökull is underlain by the mid-Atlantic-ridge, which spreads at a half rate of about 1 cm/yr [*LaFemina et al*., 2005; *Jónsson*, 2008], and by the Icelandic hot spot, coincident with the ridge. GIA following the last deglaciation ended at ∼9000 BP [*Sigmundsson*, 1991], reflecting the thermal influence of the spreading ridge and hot spot, and the corresponding low viscosity of the Icelandic upper mantle. Vatnajökull started its most recent retreat at the end of the little ice age, ∼1890 [*Sigmundsson*, 1991], when its surface area was ∼8600 km^2 [*Björnsson and Pálsson*, 2008]. From 1890 to 2003, Vatnajökull lost 435 km^3 ice. Its surface area in 2007 was ∼8100 km^2 [*Pagli et al*., 2007a, *Árnadóttir et al*., 2009]. The corresponding average thinning rate since 1890 is 0.5 m/yr (Table 1). Vatnajökull's ice loss and accumulation has varied in time, e.g., there was net growth from 1991 to 1994 [*Björnsson and Pálsson*, 2008]. The ice loss from 1994 to 2005 was 84 km^3, corresponding to an average thinning rate of 0.84 m/yr [*Björnsson and Pálsson*, 2008], almost half of the maximum rate following the last glacial maximum [2 m/yr; *Pagli and Sigmundsson*, 2008].

[8] In this section, we have reported average ice thinning rates. In the following sections, we consider spatially varying thinning rates following an exponential model, except for special cases of uniform thinning, when we quote the results of *Grapenthin et al*. [2006], and in Table 1, where we have converted the estimated mass loss rate into an average thinning rate. Throughout this paper ice thinning stands for ice elevation change.

3. Ice Mass Loss Rate Estimation From InSAR Observations

[9] Crustal uplift due to ice melting is a surface unloading problem, similar to loading the crust by water level changes in artificial or natural lakes [*Kaufmann and Amelung*, 2000; *Cavalie et al*., 2007; *Nof et al*., 2012]. We use the solution for the surface displacement of an elastic half space due to a point source with a unit mass in

Table 1. Ice Mass Loss Rates of the Vatnajökull Ice Cap and Whole Iceland

Period	Ice Loss Rate(Gt/yr)	Volume Loss (km^3)	Average Thinning Rate (m/yr)	Reference
Vatnajoekull				
1890–2003	3.5	435[a]	0.46	*Pagli et al*. [2007a] and *Árnadóttir et al*. [2009]
1994–2005	6.4	84[a]	0.84[b]	*Björnsson and Pálsson* [2008]
1995–2009	$6.8^{+0.8}_{-0.7}$	~110	~0.9[c]	This study
Whole Iceland				
2003–2010	11 ± 2[a]	84	N/A	*Jacob et al*. [2012]
1995–2010	9.5 ± 1.5	166	N/A	*Björnsson et al*. [2013]
1995–2009	10.3 ± 1	150	N/A	This study

[a]Parameter given in reference.
[b]Calculated from total thinning of 9.2 m water equivalent thickness.
[c]Calculated from the mass loss rate. Other parameters are calculated using an ice density of 917 kg/m^3 and a surface area of Vatnajökull of 8100 km^2 (post-1990).

cylindrical coordinates assuming axial symmetry [*Sneddon*, 1951; *Pinel et al*., 2007]:

$$V(r)=\frac{g}{\pi}\frac{1-\upsilon^2}{E}\frac{1}{r} \tag{1}$$

$$U(r)=\frac{g}{2\pi}\frac{(1+\upsilon)(1-2\upsilon)}{E}\frac{1}{r} \tag{2}$$

where V and U are the vertical and radial displacements, g is the gravitational acceleration, υ is the Poisson's ratio, E is the Young's modulus, and r is the distance from the point source. We assume that the load change (mass loss rate) is constant with time and use velocities instead of displacements. In the following, we formulate a linear inverse problem to estimate the load change from surface velocities.

[10] Glaciers and ice sheets generally melt from the edge toward the interior [*Sigmundsson and Einarsson*, 1992; *Marshall et al*., 2005]. We assume that the mass loss rate decreases exponentially with distance from the ice edge and describe it using the thinning rate $h(x)$,

$$h(x)=c+(a-c)e^{-x/k} \tag{3}$$

where k is the decay distance (the distance where the thinning rate reduces to 1/e of the rate at the edge), x is the distance from the ice edge, c is the thinning rate at the inland portion of a glacier ($x >> k$), and a is the thinning rate at the ice edge ($x = 0$). The units of h, a, and c are m/yr (positive for thinning), and k is in meters. Ice accumulation far from the ice edge is represented by negative c. We can expand this one-dimensional model to a two-dimensional model by dividing the load change into a series of square blocks, calculating the displacement rate due to point loads with the corresponding masses for each block, and superposing the solutions for all blocks. The ground velocities $d_l^{v,e,n}$ for such a model are calculated as

$$d_l^v=\sum_{i=1}^{N}(c+(a-c)\exp(-x_i/k))\frac{\delta^2\rho g(1-\upsilon^2)}{\pi E r_{li}} \tag{4}$$

$$d_l^{e,n}=\sum_{i=1}^{N}(c+(a-c)\exp(-x_i/k))\frac{\delta^2\rho g(1+\upsilon)(1-2\upsilon)}{2\pi E r_{li}} \tag{5}$$

where superscripts v, e, n represent vertical, east, and north directions, x_i is the distance of an ice block to the ice edge, $i = 1,\ldots, N$ with N the number of blocks, δ is the block spacing, ρ is the density of ice, and r_{li} the distance between the point load representing block i and observation point $l = 1,\ldots, L$ with L the number of observations.

[11] The ground velocity is linear with respect to parameters a and c and nonlinear with respect to k. InSAR measures velocities in the radar line-of-sight direction (LOS). For a given k, we have a linear system,

$$\mathbf{d}=\mathbf{AM} \tag{6}$$

where $\mathbf{d}=[d_1,\cdots,d_L]^T$ is the $L \times 1$ vector of observations (LOS velocities) and $\boldsymbol{m}=[a,\ c]^{\mathrm{T}}$ the 2×1 vector of model parameters. We use the least-squares solution

$$\mathbf{m}=\mathbf{A}^{-\mathrm{g}}\mathbf{d} \tag{7}$$

with $\mathbf{A}^{-\mathrm{g}}$ the generalized inverse. The model variance is given by [*Snieder and Trampert*, 1999]

$$\sigma_{m_i}^2=\sum_l\left(A_{li}^{-g}\sigma_{d_l}\right)^2 \tag{8}$$

where σ_{m_i} is the model standard error of the ith ice block, σ_{d_l} is the standard error of lth velocity field. The design matrix A can be written as

$$\mathbf{A}=\mathbf{B}\cdot\mathbf{C}\times\mathbf{D} \tag{9}$$

where **A** is a $L \times 2$ matrix, and each line represents the mapping relationship between independent variables and observation at location l. The lth line of **A** represents the mapping from mass loss rate to the lth absolute velocity field. By subtracting the line representing the reference point from each line, **A** is then a relative mapping matrix. The dot operator represents matrix elementary multiplication, and the cross operator represents matrix multiplication.

$$\mathbf{B}=\begin{bmatrix} \cos\theta_1 & \dots & \cos\theta_1 & -\sin\theta_1\cos\alpha_1 & \dots & -\sin\theta_1\cos\alpha_1 & \sin\theta_1\sin\alpha_1 & \dots & \sin\theta_1\sin\alpha_1 \\ \vdots & \vdots & \vdots & \vdots & \vdots & \vdots & \vdots & \vdots & \vdots \\ \cos\theta_L & \dots & \cos\theta_L & -\sin\theta_L\cos\alpha_L & \dots & -\sin\theta_L\cos\alpha_L & \sin\theta_L\cos\alpha_L & \dots & \sin\theta_L\cos\alpha_L \end{bmatrix} \tag{10}$$

$$C=\frac{\rho g}{\pi E}\begin{bmatrix} \frac{1-\upsilon^2}{r_{11}} & \dots & \frac{1-\upsilon^2}{r_{1N}} & \frac{(1+\upsilon)(1-2\upsilon)}{2r_{11}} & \dots & \frac{(1+\upsilon)(1-2\upsilon)}{2r_{1N}} & \frac{(1+\upsilon)(1-2\upsilon)}{2r_{11}} & \dots & \frac{(1+\upsilon)(1-2\upsilon)}{2r_{1N}} \\ \vdots & \vdots & \vdots & \vdots & \vdots & \vdots & \vdots & \vdots & \vdots \\ \frac{1-\upsilon^2}{r_{L1}} & \dots & \frac{1-\upsilon^2}{r_{LN}} & \frac{(1+\upsilon)(1-2\upsilon)}{2r_{L1}} & \dots & \frac{(1+\upsilon)(1-2\upsilon)}{2r_{LN}} & \frac{(1+\upsilon)(1-2\upsilon)}{2r_{L1}} & \dots & \frac{(1+\upsilon)(1-2\upsilon)}{2r_{LN}} \end{bmatrix} \tag{11}$$

$$\mathbf{D}=\begin{bmatrix} \exp\left(-\frac{x_1}{k}\right) & 1-\exp\left(-\frac{x_1}{k}\right) \\ \vdots & \vdots \\ \exp\left(-\frac{x_N}{k}\right) & 1-\exp\left(-\frac{x_N}{k}\right) \\ \exp\left(-\frac{x_1}{k}\right) & 1-\exp\left(-\frac{x_1}{k}\right) \\ \vdots & \vdots \\ \exp\left(-\frac{x_N}{k}\right) & 1-\exp\left(-\frac{x_N}{k}\right) \\ \exp\left(-\frac{x_1}{k}\right) & 1-\exp\left(-\frac{x_1}{k}\right) \\ \vdots & \vdots \\ \exp\left(-\frac{x_N}{k}\right) & 1-\exp\left(-\frac{x_N}{k}\right) \end{bmatrix} \tag{12}$$

[12] where **B** and **C** are 2 $L \times 3N$ matrices, in which the first N columns correspond to vertical component, the second N columns correspond to east component, and the third N columns correspond to north component. **B** contains the mapping parameters from three-dimensional velocities to LOS direction. **C** is generated from equations (4) and (5). θ is the look angle of the radar beam and α is the azimuth angle representing the flight direction. **D** is a $3N \times 2$ matrix for parameters describing the exponential unloading model.

[13] We establish a series of linear inversions by searching each possible value of k with reasonable stepping (5000 m). For a given k, we thus solve for a and c. Although the inversion problem is overdetermined, the sensitivity of the data for predicting the model varies spatially. In the far field (far from the ice edge), the data resolutions [*Menke*, 1989] are very poor. Low data resolution can bias the model predictions [*Lohman and Simons*, 2005; *Xia et al.*, 2008]. We thus use a weighting approach according to the diagonal values of the data resolution matrix $w = (\mathrm{diag}(\mathbf{N}))^p$, where w is the weighting vector, **N** is the data resolution matrix, diag() represents the process of retrieving the diagonal vector of **N**, and p is a amplification factor. We use $p = 2$ for this study.

[14] The estimated mass loss rate thus should depend on k. In practice, we find that although a and c are sensitive to k, the estimated mass loss rate is not (see section 5.). We conclude that the proposed approach allows a reliable estimation for glaciers and ice sheets with exponential thinning from edge to interior.

4. InSAR Data

[15] We use 1995–2009 C-band ERS imagery and the Small Baseline InSAR time-series method [*Berardino et al.*, 2002; *Fattahi and Amelung*, 2013] for measuring the contemporaneous deformation around Vatnajökull. In Iceland, only summer acquisitions (late June to early October) are suitable for InSAR because of snow cover during other seasons; the typical temporal density is three images per year for each track. We combine the SAR acquisitions to form interferogram networks using thresholds in perpendicular spatial baseline of 300 m and temporal baseline of 3 years, supplemented by a few longer temporal or

spatial baseline interferograms to ensure full network connection (110 and 43 interferograms on descending and ascending tracks, see supporting information[1] Figure 1). We estimate ground velocity assuming linear deformation (neglecting seasonal effects although they are known to be significant) [*Grapenthin et al*., 2006]. We eliminate long-wavelength phase contributions (the signal across the two SAR frames) by removing quadratic surfaces in range and azimuth directions, estimated at each epoch of the InSAR time-series after masking out the deforming areas near the ice edge. The long-wavelength phase contributions are due to plate motion [*LaFemina et al*., 2006; *Geirsson et al*., 2012], viscous deformation, and possibly orbital uncertainties [*Gourmelen et al*., 2010]. The effect of stratified atmospheric delays is small because of limited topographic relief in the study area. InSAR measurements, in particular at high latitudes, can be affected by ionospheric disturbances but this effect is generally small for C-band data [*Meyer*, 2011].

[17] Figures 2a and 2b show the 1995–2009 relative LOS velocities for the descending and ascending tracks. The InSAR measurements are relative to a reference point, which is a point near GPS station 7485 of *Árnadóttir et al*. [2009]. Although the relative velocities could be transferred into absolute velocities using the motion of this station, it is not needed, because our modeling approach uses relative velocities only.

[18] Figure 2 shows a 5–10 km wide yellow-red band around the southwestern edge of Vatnajökull, corresponding to relative LOS velocities up to 13 mm/yr and a large area of uplift west of the ice cap. The standard error of the LOS velocity fields are ~0.4 mm/yr and ~0.7 mm/yr for the descending and ascending tracks, respectively, estimated following *Gourmelen et al*. [2007] in an 18 × 18 km^2 nondeforming area (marked by the rectangle in Figures 2a and 2b). The displacement histories shown for two points near the ice edge suggest almost constant LOS annual velocity during the observation period (Figures 2c and 2d). Deviations up to 3 cm are most likely due to atmospheric effects and seasonal loading variations. The spatial extent of uplift is clearly represented in a map of vertical velocity (Figure 3), obtained by combining the descending and ascending LOS velocities vertical and horizontal velocities. The vertical ground velocity from InSAR is consistent with the relative changes in GPS velocities of *Arnadottir et al*. [2009] (the root-mean-square deviation is 2.1 mm/yr, see supporting information Figure 2).

[1]Additional supporting information may be found in the online version of this article.

5. Ice Mass Loss Rate Estimation

[19] We estimate the ice mass loss rate using equation (7) for thinning rate models with different decay distances k. To build matrices **B** and **C**, we represent the load change (the change of ice mass) by a series of 1.4 km^2 square blocks, each of which is approximated by a point load. We do not consider changes in surface area because the associated mass change is small. We select an area not influenced by recent volcanic activity southwest of Vatnajökull (the rectangle in Figure 4, surface area ~2500 km^2) and sample the velocity fields using a uniform grid to obtain a data vector consisting of 478 descending and 454 ascending LOS velocities. The fit of a model to the data is described by the Root Mean Square Error, $RMSE=\sqrt{\sum_{l=1}^{L}(d_l-p_l)^2/L}$, with d_l is the observations, p_l is the model predictions, and L is the number of observations. We assume unit variance for all data points.

[20] We first test an unrealistic spatially uniform thinning rate model ($k\rightarrow\infty$ in equation (3)). The solution suggests an ice mass loss rate of 20.8 Gt/yr (corresponding to an average thinning rate of 2.8 m/yr), significantly higher than previous mass loss rate estimates (Table 1). This model is characterized by an RMSE of 4.3 mm/yr, suggesting a relatively poor fit to the observations, and suggesting that a spatially uniform thinning rate model is not appropriate.

[21] We next consider exponential thinning rate models. We conduct a grid search over the decay distance k, and estimate for each k the parameters a and c using equation (6), varying k from 1 to 30 km with a step size of 0.5 km. The estimated mass loss rate depending on k is 6.8–7.3 Gt/yr (Figure 5). This narrow range of 0.5 Gt/yr suggests that variations in k are largely compensated by variations of a and c. We also found that RMSE does not vary significantly with k, i.e., the data are not sufficient to resolve k. *Björnsson and Pálsson* [2008] present a thinning rate model that can approximated by an exponential model with $k = 7.5$ km, $a = 5.5$ m/yr, and $c = -1.6$ m/yr (Figure 6). We thus use $k = 7.5$ km and invert for a and c. We find $a = 3.75$ m/yr and $c = -0.75$ m/yr,

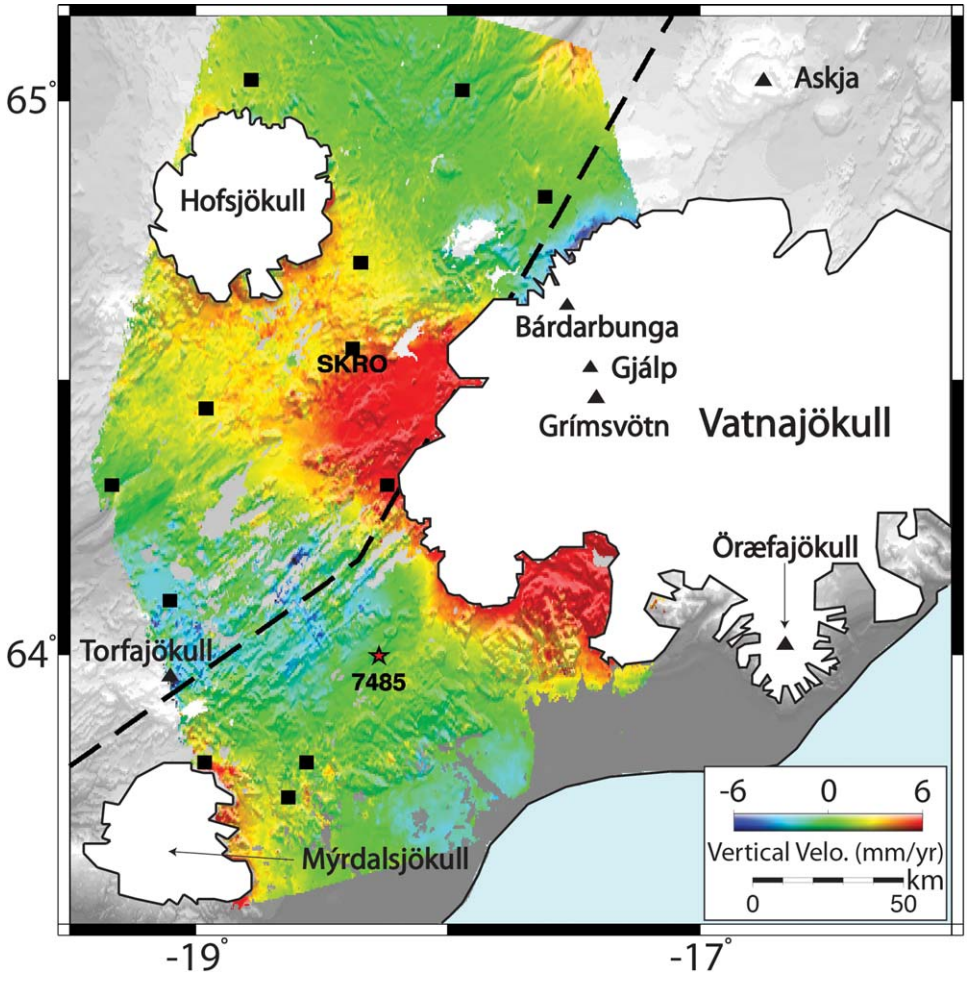

Figure 3. Vertical velocity map derived from descending and ascending LOS velocity fields. Dashed line: axis of mid-Atlantic-ridge. Red star: reference point. Black squares: GPS stations. SKRO: a continuous GPS station. Black triangles are volcanoes.

similar to values calculated by *Björnsson and Pálsson* [2008].

[22] Including the observation error, the estimated range of mass loss rate is $6.8^{+0.8}_{-0.7}$ Gt/yr. Adding the uncertainties associated with bounds in Young's modulus (40 ± 15 GPa) [*Grapenthin et al*., 2006], the estimated mass loss rate is $6.8^{+3.3}_{-3.2}$ Gt/yr.

[23] Figure 4 shows the comparison between the model with $k = 7.5$ km and the observations. In the area southwest of Vatnajökull, the model predictions closely resemble the observations (Figures 4c and 4f). Some areas with high residuals are addressed below (section 6.1).

[24] For the Hofsjökull (surface area 925 km^2) and Mýrdalsjökull (600 km^2) ice caps we also use exponential thinning rate models, invert for the mass loss rate and obtain rates of 0.9 and 1.7 Gt/yr, respectively. The estimate for Hofsjökull is close to that of *Grapenthin et al*. [2006] (their average thinning rate of 1 m/yr for 1996–2001 corresponds to a mass loss rate of 0.85 Gt/yr), but not the estimate for Mýrdalsjökull. *Grapenthin et al*. [2006] report an average thinning rate of 0.5 m/yr which corresponds to a mass loss rate of 0.3 Gt/yr. The estimates of the smaller ice caps are not well constrained because of the depth variation of Young's modulus (see section 6.3.). For Langjökull (950 km^2), we use the average thinning rate of 1.3 m/yr of *Grapenthin et al*. [2006], which corresponds to a mass loss rate of 0.9 Gt/yr, 1996–2004.

6. Discussion

6.1. Model Fit

[25] Here we investigate discrepancies between our model predictions and observations. First,

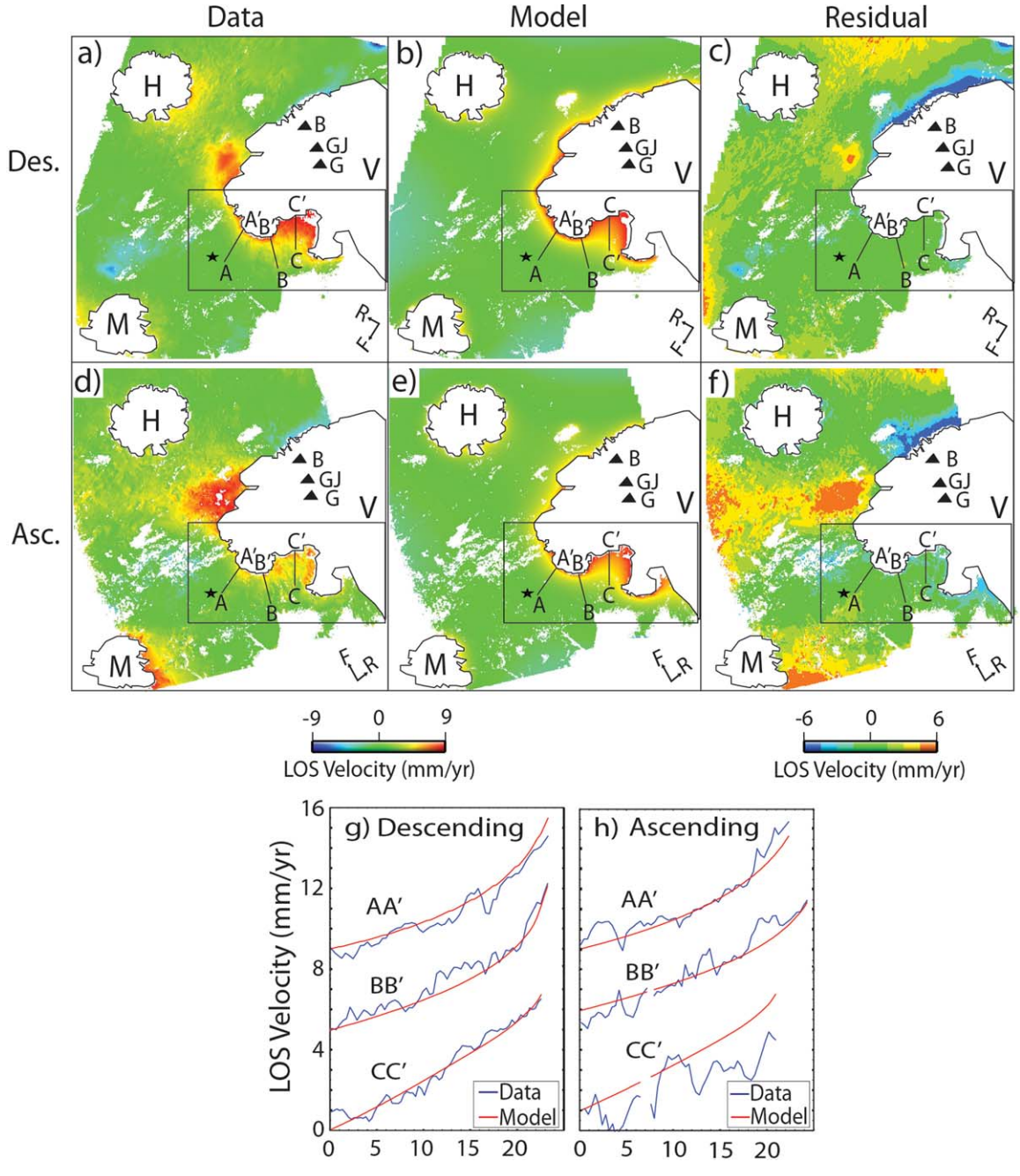

Figure 4. (a and d) Observations, (b and e) models, and (c and f) residuals. The modeled velocities were calculated for decay distance $k = 7.5$ km. Star: reference point. Black triangles: areas used for modeling. (g and h) LOS velocities along profiles for descending and ascending track. The AA′ and BB′ profiles are shifted by several mm/yr. The descending track generally fits the model better than the ascending track because of more interferograms generated on this track. B: Bardarbunga volcano, G: Grimsvötn volcano, GJ: Gjalp volcano, H: Hofsjökull ice cap, M: Mýrdalsjökull ice cap, and V: Vatnajökull ice cap. Red star: reference point.

there is a lack of observed uplift at the northwestern edge of Vatnajökull. This is an area of highest topographic elevation where melting is slow because of low air temperature [*Björnsson and Pálsson*, 2008]. This is not represented by our simple thinning rate model. This area was also subjected to subsidence following the 1996 eruption of Gjalp subglacial volcano [*Pagli et al.*, 2007b]. Discrepancies near the Hofsjökull and Myrdalsjökull ice caps are also likely due to simplification of the assumed thinning rate model. For these small ice caps, the exponential model may

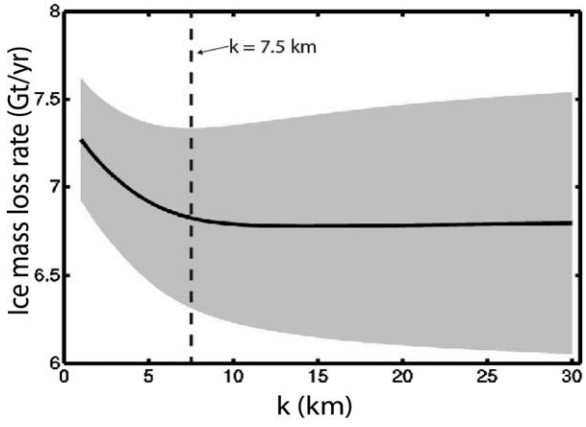

Figure 5. Ice mass loss rate as a function of the decay distance k. The gray-shaded area marks the uncertainties range which is calculated based on equation (8). Dashed line marks the preferred model at $k = 7.5$ km.

not fit very well because of the large contribution of outlet glaciers. Third, there is an excess uplift (Figure 4) west of Vatnajökull, also noted by *Árnadóttir et al*. [2009]. This area is located above and west of the spreading center. A possible explanation for excess uplift here is viscoelastic deformation related to a locally low effective elastic layer thickness. The data from these areas are not included in the modeling and do not affect the estimated ice mass loss rate.

6.2. Effect of Viscoelastic Behavior

[26] Our approach to mass loss estimation is based on the assumption that the observed relative uplift can be explained by rebound of a homogeneous elastic half-space. However, GIA has both elastic and viscous components due to viscous flow in the upper mantle and possibly in the lower crust. Modeling of GPS observations suggest that Icelandic lithosphere has a high viscosity lower crust and a low viscosity upper mantle, with average viscosities of $>10^{21}$ Pa·s and 10^{19} Pa·s, respectively, and a crustal thickness of 40 km [e.g., *Árnadóttir et al*., 2009]. *Auriac et al*. [2013] show that this rheological structure holds for the larger Vatnajökull area. However, spatial variations in rheology are likely. Iceland is located on a mid-ocean ridge and a hot spot. The lower crust and upper mantle can be thermally weakened depending on location [e.g., *Barnhoorn et al*., 2011]. For the ridge area in southwestern Iceland, *Jónsson* [2008] finds lower crustal and upper mantle viscosities of 10^{19} Pa s and 3–4 $\times$ 10^{18} Pa·s, respectively. *LaFemina et al*. [2005] find near Vatnajökull a stronger lower lithosphere (10^{19} to 10^{20} Pa s), which may reflect an increased crustal thickness. For most of Iceland, the seismic crustal thickness is 30–40 km; it is thickest under Vatnajökull and thins to 20 km in the southwest [*Foulger and Natland*, 2003].

[27] To assess the potential impact of these effects, we compute the effect of viscoelastic relaxation on the deglaciation-induced uplift using the 3D version of the finite element code GTecton [*Govers and Wortel*, 2005]. We try the effects of two different models—one with a 40 km elastic plate and half-space viscosity of 10^{18} Pa·s (model A) and a second one with a thinner elastic layer over a viscoelastic half space with a higher viscosity (5 km elastic plate and half-space viscosity of 10^{19} Pa·s, model B). Model A is similar to the model of *Auriac et al*. [2013] but has a lower viscosity, simulating the effect of elevated temperature due to the mid-ocean ridge. Model B has a low lower crustal (5–40 km) viscosity, which could be the result of high water content or nonlinear rheology. We use a time-variable, constant disk load to simulate a realistic deglaciation history (see caption of Figure 7 for details of the load).

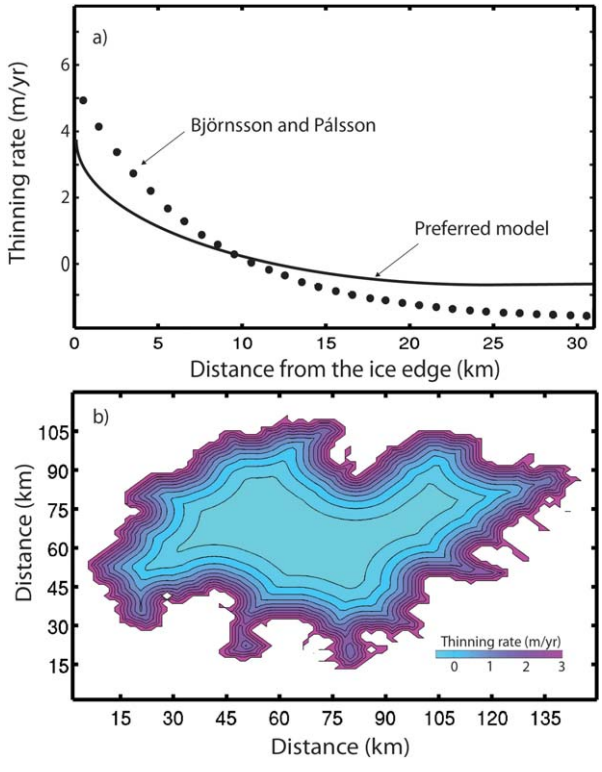

Figure 6. Thinning rate model of Vatnajökull. (a) Solid line: 1-D estimated model for $k = 7.5$ km ($a = 3.75$ m/yr, $c = -0.75$ m/yr) and dotted line: exponential approximation to the model form *Björnsson and Pálsson* [2008] ($k = 7.5$ km, $a = 5.5$ m/yr, and $c = -1.6$ m/yr). (b) two-dimensional thinning rate model obtained using the estimated 1-D model.

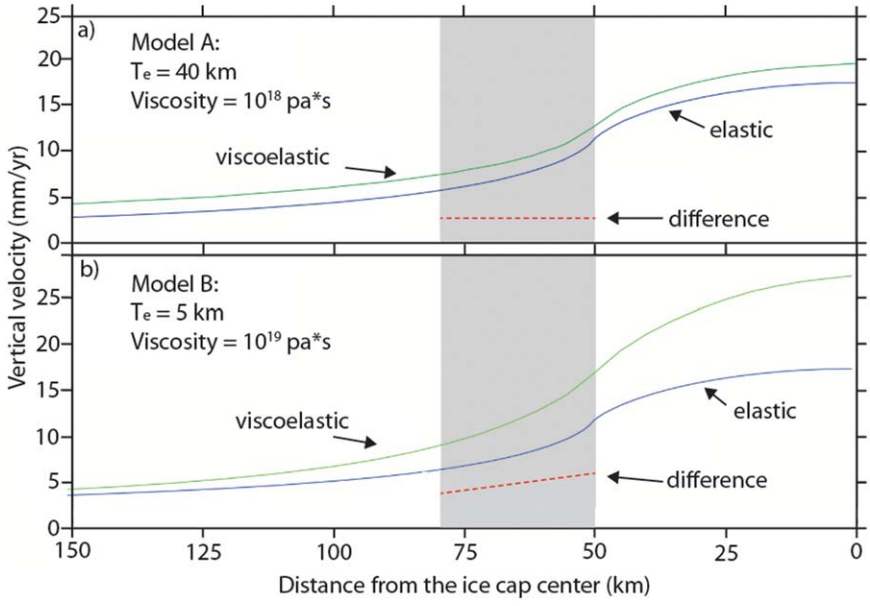

Figure 7. Simulated 1995–2009 vertical velocities for disk (50 km radius) unloading of the lithosphere along a radial profile from the disk center to 150 km distance for two different Earth models. (a) Model A: 40 km elastic layer and 10^{18} Pa·s half-space viscosity. (b) Model B: 5 km elastic layer and 10^{19} Pa·s half-space viscosity; Deglaciation starts in 1890 with thinning rates of 25, 40, and 84 cm/yr for 1890–1964, 1965–1994, and 1995–2009, respectively. Blue line: elastic response. Green line: viscoelastic response. Red dashed line: difference between blue and green lines. Gray region: area of InSAR observations at 50–80 km distance from the disk center.

[28] For model A, the elastic and viscoelastic responses are similar. The viscous component produces a constant offset of 2 mm/yr (red dashed line in Figure 7a) without affecting the uplift gradient. For model B, the viscous component decreases from 10 mm/yr at the load center to 1 mm/yr at 150 km distance (Figure 7b). It contributes ~2.5 mm/yr to the uplift gradient at 50–80 km distance. Our approach of eliminating long-wavelength deformation further lessens the impact of possible viscous deformation because it is largely removed from the observations. Weighting based on data resolution further reduces the magnitude of these viscous effects because areas with higher viscous than elastic deformation (far from the ice edge) receive less weight.

[29] We conclude that for modeling relative uplift near the ice edge the viscous component can safely be neglected, except in the case of a very weak lithosphere and a thin elastic layer. In this case, the elastic half-space assumption (i.e., neglecting viscous deformation) would lead to an overestimation of the mass loss rate, with the actual rates being smaller than the estimates. In other words, except for this very special situation, relative InSAR observations at the ice edge are mainly sensitive to the elastic component but not to the viscous component of surface deformation associated with melting ice. Of course, InSAR can only resolve mass loss at the edge of glaciers and ice sheets.

[30] The low viscosities of Model B are unlikely to occur under Iceland for two reasons. First, the upper mantle is relatively dry [*Barnhoorn et al.*, 2011] and there is no water that could act to reduce the viscosity. Second, for typical grain sizes of mid-ocean ridge mantle rock and for relatively low deglaciation-induced strain rates, linear diffusion creep is likely the dominant deformation mechanism [*Barnhoorn et al.*, 2011].

6.3. Young's Modulus

[31] Our model assumes a Young's modulus of 40 GPa. It is important to justify this assumption because surface displacement is proportional to the load and inversely proportional to Young's modulus (equations (1) and (2)). An inversion with twice the value of the Young's modulus would yield twice the mass loss rate.

[32] This modulus was estimated from GPS observations of the vertical deformation associated with

seasonal loading in Iceland (winter snowfall and summer melting) [*Grapenthin et al*., 2006]. It can be considered an effective Young's modulus for the elastic crust sampled by the load. For smaller loads, the effective Young's modulus could be smaller because the shallow crust is likely to be more fractured, hence weaker. For example, *Pinel et al*. [2007] found an effective Young's modulus of 29 GPa for the smaller Myrdalsjökull ice cap, suggesting that also the load change due to melting is of smaller spatial extent than for Vatnajökull. For larger seasonal loads significantly larger effective Young's moduli are found [*Bevis et al.*, 2005; *Steckler et al.*, 2010].

[33] For the Icelandic crust, the mean P-wave velocities of 6.0 and 6.6 km/s at depths of 5 and 10 km [from *Yang and Yang*, 2005] correspond to dynamic modulii of 87 and 105 GPa, respectively (using a density of 2900 kg/m^3 and Poisson's ratio of 0.25). Our choice of Young's modulus is significantly lower than these values and is more likely representative of conditions associated with relatively slow load changes induced by glacial melting compared to higher values estimated from the passage of seismic waves.

[34] Our values is consistent with the effective Young's modulus of 44 GPa of *Nof et al*. [2012] from modeling uplift induced by rapid decline of the Dead Sea water level. The Dead Sea load change (∼15 km across) is similar in size to the Vatnajökull load change ($k = 7.5$ km).

6.4. Mass Loss Rate

[35] For the 1995–2009 period, the mass loss rate of the Vatnajökull ice cap estimated from the InSAR data is (depending on k) $6.8^{+0.8}_{-0.7}$ Gt/yr. Mass loss rates from this and previous studies are summarized in Table 1. Our estimate agrees with the 1994–2005 rate of 6.4 Gt/yr from *Björnsson and Pálsson* [2008]. A limitation of our study is that we only use observations from the southeast edge of the ice cap. That our mass loss rate estimate agrees with the in situ observations suggests that this section is melting at the average rate of the ice cap. The estimated mass loss is about twice the average mass loss rate of 3.5 Gt/yr from 1890 to 2003 [*Pagli et al*., 2007a]. The rather constant uplift velocity during 1995–2009 (Figures 2c and 2d) suggests ice loss at a constant rate, in contrast to Greenland where ice loss is accelerating [*Jiang et al*., 2010; *Rignot et al*., 2011a].

[36] We estimate mass loss rates for the Hofsjökull and Myrdalsjökull ice caps of 0.9 and 1.7 Gt/yr. Together with Langjökull's mass loss rate of 0.9 Gt/yr, the total loss rate for the four major Icelandic ice caps (Vatnajökull, Hofsjökull, Myrdalsjökull, and Langjökull) is 10.3 ± 1 Gt/yr. This is equivalent to the 11 ± 2 Gt/yr estimated from 2003 to 2010 GRACE data [*Jacob et al*., 2012].

7. Conclusions

[37] We have presented an approach to estimate ice loss from uplift measurements of the Earth's crust near glaciers and ice sheets that is optimized for the high spatial resolution of InSAR. The linear relationship between surface load change and ground uplift for elastic rheology allows us to estimate the ice mass loss rate from the measured uplift as long as prior information on Young's modulus and the spatial thinning pattern of ice is available. An exponential decrease in thinning rate with distance from the ice edge is applicable for many glaciers and ice sheets. Our InSAR-based approach resolves small-wavelength, relative changes in uplift across a SAR frame, and is especially sensitive to contemporaneous load changes along the ice edge. It is presumably also applicable to systems dominated by ice loss near the terminus, e.g., systems undergoing the initial stages of rapid retreat (later stages may be dominated by dynamic effects and mass loss farther from the terminus). Spatial variations in ice loss due to variations in air temperature or precipitation and variable outlet glacier geometry can in principle be resolved by separately analyzing different sections of ice.

[38] For Vatnajökull, we find for the 1995–2009 period an average ice mass loss rate of $6.8^{+0.8}_{-0.7}$ Gt/yr consistent with ground-based estimates and broadly consistent with GRACE estimates for the entire island. We used only observations from the southwestern ice edge, suggesting that mass loss in this area is representative of the entire ice cap.

Acknowledgments

[39] The National Aeronautics and Space Administration Earth Science division supported this study with grants to F.A., T.D., and S. W. We thank two anonymous reviewers for their constructive comments.

References

Árnadóttir, T., B. Lund, W. Jiang, H. Geirsson, H. Björnsson, P. Einarsson, and T. Sigurdsson (2009), Glacial rebound and plate spreading: Results from the first countrywide GPS

observations in Iceland, *Geophys. J. Int.*, *177*, 691–716, doi: 10.1111/j.1365-246X.2008.04059.x.

Auriac, A., K. H. Spaans, F. Sigmundsson, A. Hooper, P. Schmidt, and B. Lund (2013), Iceland rising: Solid Earth response to ice retreat inferred from satellite interferometry and viscoelastic modeling, *J. Geophys. Res.*, *118*, 1331–1344, doi:10.1002/jgrb.50082.

Barnhoorn, A., W. van der Wal, and M. R. Drury (2011), Upper mantle viscosity and lithospheric thickness under Iceland, *J. Geodyn.*, *52*, 260–270, doi:10.1016/j.jog.2011.01.002.

Berardino, P., G. Fornaro, R. Lanari, and E. Sansosti (2002), A new algorithm for surface deformation monitoring based on small baseline differential SAR interferograms, *IEEE Trans. Geosci. Remote Sens.*, *40*, 2375–2383, doi:10.1109/TGRS.2002.803792.

Bevis, M., D. Alsdorf, E. Kendrick, L. Fortes, B. Forsberg, R. Smalley Jr., and J. Becker (2005), Seasonal fluctuations in the mass of the Amazon River system and Earth's elastic response, *Geophys. Res. Lett.*, *32*, L16308, doi: 10.1029/2005GL023491.

Bevis, M., et al. (2012), Bedrock displacements in Greenland manifest ice mass variations, climate cycles and climate change, *Proc. Natl. Acad. Sci. U. S. A.*, *109*(30), 11,944–11,948, doi:10.1073/pnas.1204664109.

Björnsson, H., and F. Pálsson (2008), Icelandic glaciers, *Jökull*, *58*, 365–386.

Björnsson, H., F. Pálsson, S. Gudmundsson, E. Magnússon, G. Adalgeirsdóttir, T. Jóhannesson, E. Berthier, O. Sigurdsson, and T. Thorsteinsson (2013), Contribution of Icelandic ice caps to sea level rise: Trends and variability since the Little Ice Age, *Geophys. Res. Lett.*, *40*, 1–5, doi:10.1002/grl.50278.

Cavalie, O., M.-P. Doin, C. Lasserre, and P. Briole (2007), Ground motion measurement in the Lake Mead area, Nevada, by differential synthetic aperture radar interferometry time series analysis: Probing the lithosphere rheological structure, *J. Geophys. Res.*, *112*, B03403, doi:10.1029/2006JB004344.

Chen, J. L., et al. (2006), Satellite gravity measurements confirm accelerated melting of Greenland ice sheet, *Science*, *313*, 1958–1960, doi:10.1126/science.1129007.

Chen, J. L., C. R. Wilson, D. Blankenship, and B. D. Tapley (2009), Accelerated Antarctic ice loss from satellite gravity measurements, *Nat. Geosci.*, *2*, 859–862, doi:10.1038/NGEO694.

Ewert, H., A. Groh, and R. Dietrich (2011), Volume and mass changes of the Greenland ice sheet inferred from ICESat and GRACE, *J. Geodyn.*, *59–60*, 111–123, doi:10.1016/j.jog.2011.06.003.

Fattahi, H., and F. Amelung (2013), DEM error correction in InSAR time series, *IEEE Trans. Geosci. Remote Sens.*, *99*, 1–11, doi:10.1109/TGRS.2012.2227761.

Foulger, G. R., and J. H. Natland (2003), Is ''hotspot'' volcanism a consequence of plate tectonics?, *Science*, *300*, 921–922.

Gardner, A. S., et al. (2013), A reconciled estimate of glacier contributions to sea level rise: 2003 to 2009, *Science*, *340*, 852–857, doi:10.1126/science.1234532.

Geirsson, H., P. LaFemina, T. Árnadóttir, E. Sturkell, F. Sigmundsson, M. Travis, P. Schmidt, B. Lund, S. Hreinsdóttir, and R. Bennett (2012), Volcano deformation at active plate boundaries: Deep magma accumulation at Hekla volcano and plate boundary deformation in south Iceland, *J. Geophys. Res.*, *117*, B11409, doi:10.1029/2012JB009400.

Gourmelen, N., F. Amelung, F. Casu, M. R. Manzo, and R. Lanari (2007), Minning-related ground deformation in Crescent Valley, Nevada: Implications for sparse GPS networks, *Geophys. Res. Lett.*, *34*, L09309, doi:10.1029/2007GL029427.

Gourmelen, N., F. Amelung, and R. Lanari (2010), Interferometric synthetic aperture radar-GPS integration: Interseismic strain accumulation across the Hunter Mountain fault in the eastern California shear zone, *J. Geophys. Res.*, *115*, B09408, doi:10.1029/2009JB007064.

Govers, R., and M. J. R. Wortel (2005), Lithosphere tearing at STEP faults: Response to edges of subduction zones, *Earth Planet. Sci. Lett.*, *236*, 505–523.

Grapenthin, R., F. Sigmundsson, H. Geirsson, T. Árnadóttir, and V. Pinel (2006), Icelandic rhythmics: Annual modulation of land elevation and plate spreading by snow load, *Geophys. Res. Lett.*, *33*, L24305, doi:10.1029/2006GL028081.

Howat, I. M., B. E. Smith, I. Joughin, and T. A. Scambos (2008), Rates of southeast Greenland ice volume loss from combined ICESat and ASTER observations, *Geophys. Res. Lett.*, *35*, L17505, doi:10.1029/2008GL034496.

Jacob, T., J. Wahr, W. T. Pfeffer, and S. Swenson (2012), Recent contributions of glaciers and ice caps to sea level rise, *Nature*, *482*, 514–518, doi:10.1038/nature10847.

Jiang, Y., T. H. Dixon, and S. Wdowinski (2010), Accelerating uplift in the North Atlantic region as an indicator of ice loss, *Nat. Geosci.*, *3*, 404–407, doi:10.1038/NGEO845.

Jónsson, S. (2008), Importance of post-seismic viscous relaxation in southern Iceland, *Nat. Geosci.*, *1*, 136–139, doi:10.1038/ngeo105.

Joughin, I. (2002), Ice-sheet velocity mapping: A combined interferometric and speckle-tracking approach, *Ann. Glaciol.*, *34*, 195–201, doi:10.3189/17275640278187978.

Joughin, I., I. Howat, B. Smith, and T. Scambos (2011), *MEaSUREs Greenland Ice Velocity: Selected Glacier Site Velocity Maps from InSAR*, Natl. Snow and Ice Data Cent., Digital Media, Boulder, Colo.

Kaufmann, G., and F. Amelung (2000), Reservoir-induced deformation and continental rheology in vicinity of Lake Mead, Nevada, *J. Geophys. Res.*, *105*(B7), 16,341–16,358, doi:10.1029/2000JB900079.

Khan, S. A., J. Wahr, L. A. Stearns, G. S. Hamilton, T. van Dam, K. M. Larson, and O. Francis (2007), Elastic uplift southeast Greenland due to rapid ice mass loss, *Geophys. Res. Lett.*, *34*, L21701, doi:10.1029/2007GL031468.

Khan, S. A., J. Wahr, M. Bevis, I. Velicogna, and E. Kendrick (2010), Spread of ice mass loss into northwest Greenland observed by GRACE and GPS, *Geophys. Res. Lett.*, *37*, L06501, doi:10.1029/2010GL042460.

LaFemina, P. C., T. H. Dixon, R. Malservisi, T. Árnadóttir, E. Sturkell, F. Sigmundsson, and P. Einarsson (2005), Geodetic GPS measurements in south Iceland: Strain accumulation and partitioning in a propagating ridge system, *J. Geophys. Res.*, *110*, B11405, doi:10.1029/2005JB003675.

Lenaerts, J. T., J. H. van Angelen, M. R. van den Broeke, A. S. Gardner, B. Wouters, and E. van Meijgaard (2013), Irreversible mass loss of Canadian Arctic Archipelago glaciers, *Geophys. Res. Lett.*, *40*, 870–874, doi:10.1002/grl.50214.

Liu, L., J. Wahr, I. Howat, S. A. Khan, I. Joughin, and M. Furuya (2012), Constraining ice mass loss from Jakobshavn Isbræ (Greenland) using InSAR-measured crustal uplift, *Geophys. J. Int.*, *188*, 994–1006, doi:10.1111/j.1365-246X.2011.05317.x.

Lohman, R. B., and M. Simons (2005), Some thoughts on the use of InSAR data to constrain models of surface

deformation: Noise structure and data downsampling, *Geochem. Geophys. Geosyst.*, *6*, Q01007, doi:10.1029/2004GC000841.

Marshall, S. J., H. Björnsson, G. E. Flowers, and G. K. C. Clarke (2005), Simulation of Vatnajökull ice cap dynamics, *J. Geophys. Res.*, *110*, F03009, doi:10.1029/2004JF000262.

Meier, M. F., M. B. Dyurgerov, U. K. Rick, S. O'Neel, W. T. Pfeffer, R. S. Anderson, S. P. Anderson, and A. F. Glazovsky (2007), Glaciers dominate eustatic sea-level rise in the 21st century, *Science*, *317*, 1064, doi:10.1126/science.1143906.

Menke, W. (1989), *Geophysical Data Analysis: Discrete Inverse Theory (Revised Edition)*, Academic Press.

Meyer, F. (2011), Performance requirements for ionospheric correction of low-frequency SAR data, *IEEE Trans. Geosci. Remote Sens.*, *49*(10), 3694–3702, doi:10.1109/TGRS.2011.2146786.

Mitrovica, J. X., G. A. Milne, and J. L. Davis (2001), Glacial isostatic adjustment on a rotating earth, *Geophys. J. Int.*, *147*, 562–578.

Nof, R. N., A. Ziv, M.-P. Doin, G. Baer, Y. Fialko, S. Wdowinski, Y. Eyal, and Y. Bock (2012), Rising of the lowest place on Earth due to Dead Sea water-level drop: Evidence from SAR interferometry and GPS, *J. Geophys. Res.*, *117*, B05412, doi:10.1029/2011JB008961.

Osmanoğlu, B., M. Braun, R. Hock, and F. J. Navarro (2013), Surface velocity and ice discharge of the ice cap on King George Island, Antarctica, *Annals of Glaciology*, *54*, 63, doi: 10.3189/2013AoG63A517.

Pagli, C., and F. Sigmundsson (2008), Will present day glacier retreat increase volcanic activity? Stress induced by recent glacier retreat and its effect on magmatism at the Vatnajökull ice cap, Iceland, *Geophys. Res. Lett.*, *35*, L09304, doi: 10.1029/2008GL033510.

Pagli, C., F. Sigmundsson, B. Lund, E. Sturkell, H. Geirsson, P. Einarsson, T. Árnadóttir, and S. Hreinsdottir (2007a), Glacio-isostatic deformation around the Vatnajökull ice cap, Iceland, induced by recent climate warming: GPS observations and finite element modeling, *J. Geophys. Res.*, *112*, B08405, doi:10.1029/2006JB004421.

Pagli, C., F. Sigmundsson, R. Pedersen, P. Einarsson, T. Árnadóttir, and K. L. Feigl (2007b), Crustal deformation associated with the 1996 Gjalp subglacial eruption, Iceland: InSAR studies in affected areas adjacent to the Vatnajökull ice cap, *Earth Planet. Sci. Lett.*, *259*, 24–33, doi:10.1016/j.epsl.2007.04.019.

Peltier, W. R. (1974), The impulse response of a Maxwell earth, *Rev. Geophys. Space Phys.*, *12*(4), 651–665.

Pinel, V., F. Sigmundsson, E. Sturkell, H. Geirsson, P. Einarsson, M. T. Gudmundsson, and T. Hognadottir (2007), Discriminating volcano deformation due to magma movements and variable surface loads: Application to Katla subglacial volcano, Iceland, *Geophys. J. Int.*, *169*, 325–338, doi:10.1111/j.1365-246X.2006.03267.x.

Pritchard, H. D., R. J. Arthern, D. G. Vaughan, and L. A. Edwards (2009), Extensive dynamic thinning on the margins of the Greenland and Antarctic ice sheets, *Nature*, *461*, 971–975, doi:10.1038/nature08471.

Ramillien, G., A. Lombard, A. Cazenave, E. R. Ivins, M. Llubes, F. Remy, and R. Biancale (2006), Interannual variations of the mass balance of the Antarctica and Greenland ice sheets from GRACE, *Global Planet. Change*, *53*, 198–208, doi:10.1016/j.gloplacha.2006.06.003.

Rignot, E., J. L. Bamber, M. R. van den Broeke, C. Davis, Y. Li, W. J. van de Berg, and E. van Meijgaard (2008), Recent Antarctic ice mass loss from radar interferometry and regional climate modeling, *Nat. Geosci.*, *1*, 106–110, doi: 10.1038/ngeo102.

Rignot, E., I. Velicogna, M. r. van den Broeke, A. Monaghan, and J. Lenaerts (2011a), Acceleration of the contribution of the Greenland and Antarctic ice sheets to sea level rise, *J. Geophys. Res.*, *38*, L05503, doi:10.1029/2011GL046583.

Rignot, E., J. Mouginot, and B. Scheuch (2011b), Ice flow of the Antarctic ice sheet, *Science*, *333*, 1427, doi:10.1126/science.1208336.

Rignot, E., S. Jacobs, J. Mouginot, and B. Sceuchl (2013), Ice-shelf melting around Antarctica, *Science*, *341*, 266–270, doi:10.1126/science.1235798.

Shepherd, A., et al. (2012), A reconciled estimate of ice-sheet mass balance, *Science*, *338*, 1183–1189, doi:10.1126/science.1128102.

Sigmundsson, F. (1991), Post-glacial rebound and asthenosphere viscosity in Iceland, *Geophys. Res. Lett.*, *18*(6), 1131–1134, doi:10.1029/91GL01342.

Sigmundsson, F., and P. Einarsson (1992), Glacio-isostatic crustal movements caused by historical volume chance of the Vatnajökull ice cap, Iceland, *Geophys. Res. Lett.*, *19*(21), 2123–2126, doi:10.1029/92GL02209.

Slobbe, D. C., P. Ditmar, and R. C. Lindenbergh (2009), Estimating the rates of mass change, ice volume change and snow volume change in Greenland from ICESat and GRACE data, *Geophys. J. Int.*, *176*, 95–106, doi:10.1111/j.1365-246X.2008.03978.x.

Sneddon, I. N. (1951), *Fourier Transforms*, 542 pp., McGraw-Hill.

Snieder, R., and J. Trampert (1999), *Inverse Problems in Geophysics,* Reprinted from *Wavefield Inversion*, edited by A. Wirgin, pp. 119–190, Springer, New York.

Sørensen, L. S., S. B. Simonsen, K. Nielsen, P. Lucas-Picher, G. Spada, G. Adalgeirsdottir, R. Forsberg, and C. S. Hvidberg (2011), Mass balance of the Greenland ice sheet (2003–2008) from ICESat data—The impact of interpolation, sampling and firn density, *The Cryosphere*, *5*, 173–186, doi:10.5194/tc-5–173-2011.

Steckler, M., S. L. Nooner, S. H. Akhter, S. K. Chowdhury, S. Bettadpur, L. Seeber, and M. G. Kogan (2010), Modeling Earth deformation from monssonal flooding in Bangladesh using hydrographic, GPS, and Gravity Recovery and Climate Experiment (GRACE) data, *J. Geophys. Res.*, *115*, B08407, doi: 10.1029/2009JB007018.

Velicogna, I., and J. Wahr (2006), Acceleration of Greenland ice mass loss in spring 2004, *Nature*, *443*, 329–331, doi: 10.1038/nature05168.

Wouters, B., D. Chambers, and E. J. O. Schrama (2008), GRACE observes small-scale mass loss in Greenland, *Geophys. Res. Lett.*, *35*, L20501, doi:10.1029/2008GL034816.

Wu, P. (1992), Deformation of an incompressible viscoelastic flat earth with power-law creep: A finite element approach, *Geophys. J. Int.*, *108*, 35–51.

Xia, J., R. D. Miller, and Y. Xu (2008), Data-resolution matrix and model-resolution matrix for Rayleigh-wave inversion using a damped least-squares method, *Pure Appl. Geophys.*, *165*, 1227–1248, doi:10.1007/s00024-008-0364-2.

Yang, Q., S. Wdowinski, and T. Dixon (2013), Annual variation of coastal uplift in Greenland as an indicator of variable and accelerating ice mass loss, *Geochem. Geophys. Geosyst.*, *14*, 1569–1589, doi:10.1002/ggge.20089.

Yang, T., and S. Yang (2005), P-wave velocity structure of the crust and uppermost mantle beneath Iceland from local earthquake tomography, *Earth Planet. Sci. Lett.*, *235*, 597–609.